



Gold-incorporated porous hollow carbon nanofiber for reversible magnesium-metal batteries

Seongsoo Lee^a, Dong Woo Kang^b, Jin Hwan Kwak^{a,c}, Sunghee Shin^{a,c}, Jun-Woo Park^b,
Seung-Ho Yu^c, Hun-Gi Jung^{a,d}, Byung Gon Kim^{b,*}, Hee-Dae Lim^{a,d,*}

^a Energy Storage Research Center, Korea Institute of Science and Technology (KIST), Seoul 02792, Republic of Korea

^b Next Generation Battery Research Center, Korea Electrotechnology Research Institute (KERI), Changwon-si 51543, Republic of Korea

^c Department of Chemical and Biological Engineering, Korea University, Seoul 02841, Republic of Korea

^d Division of Energy & Environment Technology, KIST School, Korea University of Science and Technology (UST), Seoul 02792, Republic of Korea

ARTICLE INFO

Keywords:

Magnesium-metal battery
Anode
Carbon nanofiber
Nucleation seed
Gold nanoparticles

ABSTRACT

Rechargeable magnesium-metal batteries have received ever-increasing attention as potential alternatives to current Li-ion batteries. Although the most relevant studies have mainly focused on exploring compatible electrolyte and cathode materials, relatively less attention has been paid to the development of an efficient anode host. Herein, we propose a unique anode host with a porous hollow carbon nanofiber structure and gold nanoparticles incorporated in the interior (Au@PCNF). Using the dual-nozzle electrospinning technique, a porous web body was configured with the hierarchical network of hollow carbon nanofibers, with the interior of each string specially designed to embed Au nanoparticles. We demonstrated that Au nanoparticles can act as magnesiophilic sites for Mg plating; therefore, we decorated the magnesiophilic seeds inside the hollow nanofibers to efficiently attract newly deposited Mg metal. The unique feature of Au@PCNF not only reduced the nucleation overpotentials for Mg plating but also guided the even deposition of Mg metal on the substrate. As a result, Au@PCNF exhibited stable and long-term cycle performance with enhanced adhesion property for the newly deposited Mg metal compared with other controls. This novel structural design is promising for the development of efficient anode hosts for magnesium-metal batteries, which will help open an avenue for the practical application of multivalent-ion batteries.

1. Introduction

Rechargeable Li-ion batteries (LIBs) have brought great successes in the last few decades, conquering most of the markets for commercial and portable electronic devices as a primary energy-supplying source.[1,2] In addition, they are expected to power the upcoming energy-storage-device markets such as electric vehicles (EVs) and energy storage systems (ESSs).[3–5] However, as future applications become more demanding in terms of energy density combined with high safety, current LIBs are not expected to sufficiently satisfy the demands of this fast-growing market.[6–8] In this respect, intensive research efforts have been devoted to the exploration of a new key player, which can potentially overcome the prevailing issues faced by current LIBs. Among the proposed next-generation batteries, magnesium (Mg)-metal batteries (MMBs) stand out as promising candidates that can potentially be

applied for large-scale EVs and ESSs owing to attractive features such as a high volumetric capacity of 3833 mAh/cm³ (vs. 2046 mAh/cm³ for Li metal), non-toxicity, cost-effectiveness given the natural abundance of the raw materials, and environmentally friendly sources.[9–11] In addition, Mg metal suffers less from dendritic metal growth relative to Li metal, which can be greatly advantageous, especially in terms of battery safety.[12–14] It is because the diffusion barrier of the Mg atom is relatively small, enabling preferential growth along with a surface to suppress dendritic Mg growth.[15,16]

After the first discovery of rechargeable MMBs,[9] most research has mainly focused on the exploration of appropriate electrolytes and cathodes for their practical use.[12,17–24] There have been great advances in the development of electrolytes that are compatible with Mg metal with acceptable voltage windows and reversible Mg plating/stripping, including Grignard-based electrolytes, organoborate-based

* Corresponding authors at: Next Generation Battery Research Center, Korea Electrotechnology Research Institute (KERI), Changwon-si 51543, Republic of Korea (B.G. Kim); Energy Storage Research Center, Korea Institute of Science and Technology (KIST), Seoul 02792, Republic of Korea (H.-D. Lim).

E-mail addresses: byunggonkim@keri.re.kr (B. Gon Kim), hdlim@kist.re.kr (H.-D. Lim).

<https://doi.org/10.1016/j.cej.2021.133968>

Received 23 October 2021; Received in revised form 26 November 2021; Accepted 29 November 2021

Available online 3 December 2021

1385-8947/© 2021 The Author(s).

Published by Elsevier B.V. This is an open access article under the CC BY-NC-ND license

(<http://creativecommons.org/licenses/by-nc-nd/4.0/>).

electrolytes, and Mg aluminate chloride complexes [9,25,26] In addition, various cathode materials for efficiently accommodating multivalent Mg^{2+} ions have been proposed, and excellent cathode materials of Chevrel phases (Mo_6X_8 ; $X = S, Se, Te$) have been developed. [27–29] In contrast, relatively less attention has been paid to the investigation of suitable anodes for MMBs. Nevertheless, identifying an appropriate anode host is also critical for the practical application of MMBs. In addition, it has recently been demonstrated that newly deposited Mg metal is prone to detach on conventional metal substrates, even on a Mg-metal anode. [30,31] Therefore, it is urgent to explore new anode hosts that can achieve reversible Mg plating/stripping with high adhesion of the deposited Mg metal.

In this study, we propose a novel anode host consisting of porous carbon nanofibers (PCNFs) with gold nanoparticles (Au NPs) incorporated inside the shell (*i.e.*, Au@PCNF) for rechargeable MMBs. Using the dual-nozzle electrospinning technique, the core-shell structure of Au@PCNF consisting of the three-dimensional (3D) porous main body with numerous hollow nanofibers was configured, and each fiber was specially designed to embed Au NPs inside the shell. The unique structure of Au@PCNF in combination with the catalytically magnesiophilic sites resulted in improved reversibility for the Mg plating/stripping process as well as high affinity toward Mg metal. This work aims to report the unique anode host of Au@PCNF with superior Mg storage performance while also highlighting the importance of adopting appropriate anodes for practical MMBs.

2. Results and discussion

To design the unique structure of Au@PCNF, we fabricated a 3D porous architecture consisting of a main PCNF body decorated by Au NPs inside the fibers. As schematically illustrated in Fig. 1a, two types of polymers were simultaneously electrospun using the dual-nozzle system to produce the hollow feature of the PCNFs: a core polymer solution was prepared by mixing a thermal-decomposable polymer material with the Au precursor, and a carbonizable polymer precursor was used as the shell polymer solution. The as-electrospun polymer fibers possessed a high-aspect-ratio with an average diameter of ~ 1 μm (Fig. S1). Through stepwise heat treatment up to 850 $^{\circ}C$ in an Ar atmosphere, the as-

electrospun polymer was converted into carbon fibers, and then, the core-shell structured Au@PCNF were finally obtained.

The dual nozzles enabled the production of the unique core-shell structure, with individually different properties for each core and shell material. During the heat treatment, the core polymers were mostly thermally decomposed, resulting in the formation of empty core volumes. At the same time, the Au precursor, which was co-mixed with the core polymer solution, could be thermally reduced to the metallic Au NPs and they could be naturally saved in the empty core. In the meantime, the shell polymers transformed into the outer carbon shell during the carbonization process. Each polymer solution contained a porogen, which played a key role in generating pores in the shell surface. Because of the porogen decomposition in gas form during the heat treatment, numerous pores in both the core and shell parts were generated, as illustrated in Fig. 1a.

After the heat treatment, the diameter of each fiber was reduced to ~ 500 nm; however, its overall porous 3D shape was well-maintained (Fig. 1b). The generated holes on the fiber surface were clearly observed in scanning electron microscopy (SEM) images (Fig. 1c), and the shell pores had nano-scale diameters (Figs. S2 and S3). In addition, the transmission electron microscopy (TEM) and energy-dispersive X-ray spectroscopy (EDS) images show that the Au NPs successfully formed inside the fibers with uniform diameters of 20–30 nm (Fig. 1d–f). The lattice spacing of 2.35 Å corresponding to the Au (111) plane (inset of Fig. 1e) as well as the X-ray diffraction pattern (Fig. S4) confirmed the formation of the metallic Au NPs. Moreover, thermogravimetric analysis (TGA) revealed that Au NPs accounted for ~ 1.5 wt% in the Au@PCNF (Fig. S5), and the Brunauer–Emmett–Teller (BET) surface areas of Au@PCNF and PCNF were measured to be 16.2 and 17.7 m^2/g (Fig. S6), respectively.

There are three important design rules in the fabrication of Au@PCNF. (1) We used Au NPs as heterogeneous seeds because they are expected to act as magnesiophilic hosts for Mg plating. If a heterogeneous seed forms a solid solution with the target metal (*e.g.*, Li), [32] it could reduce the nucleation overpotential by forming a solid-solution buffer layer on the surface. Similarly, we believe that the use of metal seeds may guide a favorable Mg deposition; however, there are no reports for guided Mg deposition to the best of our knowledge. Because Au

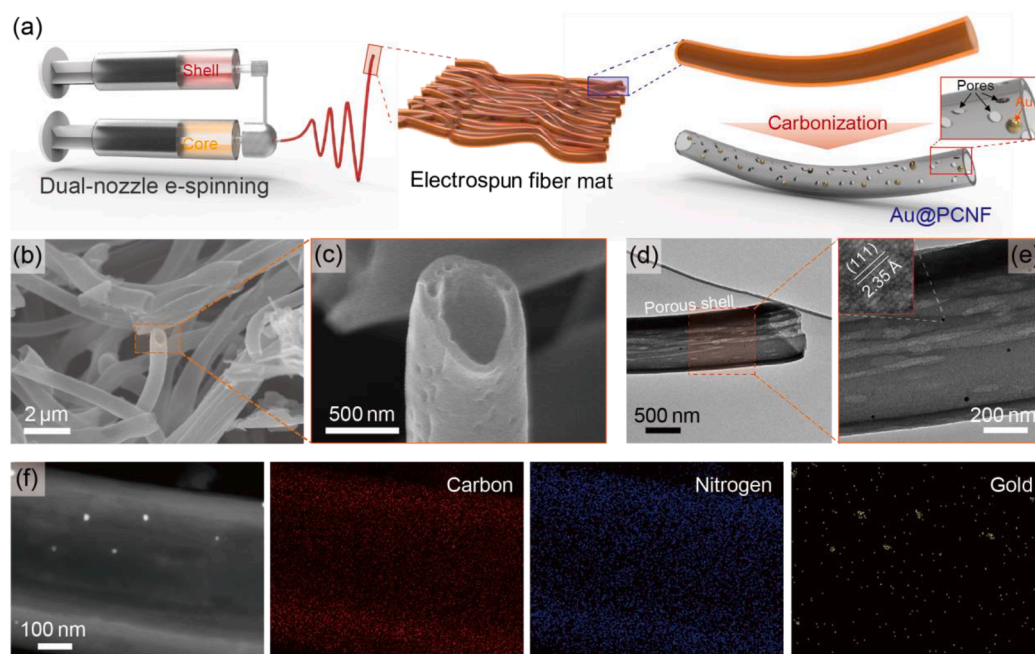


Fig. 1. (a) Schematic illustration of synthesis of Au@PCNF. (b,c) SEM images of electrospun Au@PCNF after carbonization. (d,e) TEM images of Au@PCNF and (f) corresponding EDS elemental mapping.

is known to form alloys with Mg,[33,34] it is expected to reduce the nucleation overpotential for Mg deposition. (2) Au NPs were intentionally decorated inside of each fiber. This unique feature is advantageous for preventing undesirable detachment of the heterogeneous seed during cycles and may provide resistance to the fatal dendritic growth, as similarly approached for LIBs.[35–39] (3) All the produced PCNFs were designed to have enough holes on the shell surfaces with the well-distributed features (Fig. 1c–e). We expected that the hollow PCNFs may provide fast pathways for the transport of ions into the fibers. Then, the channels will guide Mg depositions preferentially on Au seeds placed inside the wall.

The effect of the fabricated Au@PCNF was electrochemically investigated compared with a Cu substrate and PCNF without Au NPs. In a half-cell configuration, Mg metal was electrochemically deposited on each substrate at a current density of 0.2 mA/cm² (Fig. 2a–c). As observed in the galvanostatic discharge profiles, all the substrates showed a voltage dip at the beginning of Mg plating, followed by a flat voltage plateau. The difference between the initial lowest value and the flat voltage plateau is designated as the nucleation overpotential for Mg metal plating. Although an initial nucleation overpotential of 264.5 mV was observed on the Cu substrate, it was reduced on PCNF (164.8 mV) and greatly decreased on Au@PCNF (149.8 mV). In addition, the saturated voltage plateau was lower for Au@PCNF (24.6 mV) compared with those for PCNF (26.0 mV) and the Cu substrate (27.8 mV). It should be noted that the decreased nucleation overpotentials for the PCNFs are due to the higher surface areas compared with the flat Cu substrate, and the catalytic edges of carbon surfaces may help to attract cations.[31] More importantly, the most favorable Mg plating ability on Au@PCNF could be attributed to the magnesiophilic Au seeds, which will be proved and discussed later.

The adhesion property of each substrate for the newly deposited Mg was investigated. In Fig. 2d–f, digital photograph images of each substrate (Cu, PCNF, and Au@PCNF) and separator after electroplating Mg metal to 5 mAh/cm² are presented. For the Cu substrate, both the separator (right image) and substrate (left image) were greatly clogged with Mg deposits (Fig. 2d). This result was observed because the newly deposited Mg exhibited very poor adhesion toward the Cu substrate, implying that the growth of Mg metal on 2D foil is unfavorable and that the Mg is easily detachable. Similarly, it has been reported that electrochemically deposited Mg metal is prone to detach from substrates.[30,31] Although the adhesion property appeared to be improved somewhat for PCNF, top-plated Mg metal on the substrate was partially observed (left image in Fig. 2e), and the separator faced with PCNF was still partially clogged with Mg metal. Notably, we observed that the Au@PCNF substrates exhibited noticeably different morphologies after the Mg depositions (Fig. 2f). The original morphological appearance of Au@PCNF was well-preserved, and the separator appeared clean after the same amount of Mg plating. This result indicates that Au@PCNF is superior in accommodating newly deposited Mg metal with improved adhesion property. Considering that both the PCNF and Au@PCNF have structurally similar volumes for hosting Mg deposits, it is reasonable to conclude that the decorated Au NPs contributed to the preferential Mg deposition.

To directly determine whether Au NPs act as magnesiophilic seeds, we performed a Mg plating test using a Au-patterned Cu substrate (Fig. 2g–h). Using a sputter coater, Au NPs were sputtered in diamond-shaped patterns on the Cu substrate (Fig. 2g), and then, the prepared substrate was electroplated with Mg metal at a current density of 0.2 mA/cm² for 30 min. The SEM and EDS analyses in Fig. 2h prove that Mg metal was preferentially deposited onto the diamond-shaped area where

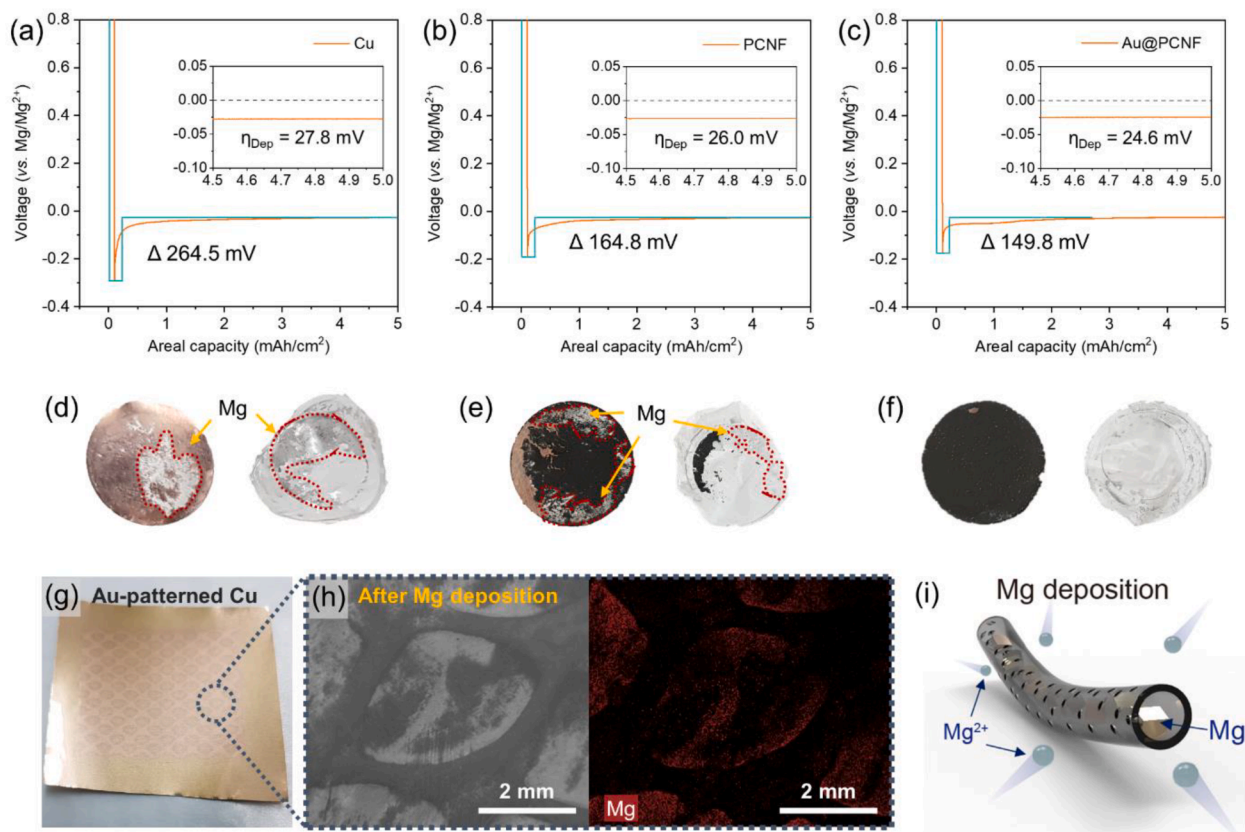


Fig. 2. Nucleation polarizations for Mg deposition on various substrates: (a) Cu, (b) PCNF, and (c) Au@PCNF at a current density of 0.2 mA/cm². (d–f) Photographs of each substrate (left image: (d) Cu, (e) PCNF, and (f) Au@PCNF) and (right image) separator in the cell after Mg plating to 5 mAh/cm² at a current density of 0.2 mA/cm². (g) Photograph of Au-patterned Cu substrate and (h) SEM image and EDS mapping after Mg deposition. (i) Schematic illustration showing Mg deposition behavior in Au@PCNF during Mg plating process.

Au was pre-patterned, whereas the bare Cu substrate remained clean. This result clearly verifies that Au seeds inside Au@PCNF induce the favorable Mg deposition, guided by the numerous surface pores, as schematically illustrated in Fig. 2i.

The Mg hosting ability of Au@PCNF was further investigated by analyzing the electrodes using SEM and EDS (Fig. 3). Each substrate (Cu, PCNF, and Au@PCNF) was prepared in a half-cell configuration, and Mg metal was deposited to 5 mAh/cm² at 0.2 mA/cm². On the Cu substrate, Mg metal was deposited in a largely aggregated form (Fig. 3a). The massive Mg deposits (Figs. S7 and S8) exhibited very poor adhesion to the substrate and were prone to be detached and clogged in the separator, as observed in Fig. 2d, leading to cell failure. In contrast, this large Mg lump was not observed on the PCNF (Fig. 3b); instead, much smaller-sized (<5 μm) Mg deposits were partially agglomerated (inset of Fig. 3b). Notably, such a noticeable Mg aggregate was not observed on the surface of Au@PCNF (Fig. 3c and inset), implying that the newly deposited Mg metal was well dispersed and stored in the inner space of the fibers (Fig. S9). For further investigation, we examined cross-sectional SEM images of the PCNF and Au@PCNF (Fig. 3d and e). The Mg deposits plated on PCNF appeared mostly near the top area of the electrode, whereas most of the fibers near the bottom, close to the Cu substrate, remained inactive (Fig. 3d). However, the Au seeds in Au@PCNF contributed to ideal even Mg depositions over the entire electrode depth rather than surface-oriented reactions (Fig. 3e). Additionally, SEM images of the pristine Au@PCNF before cell assembly are provided in Fig. S10. The uniform Mg depositions prevented fatal agglomeration and undesirable detachment while also enabling full use of the available hosting sites in Au@PCNF, resulting in improved electrochemical performance. These results explain why Au@PCNF exhibited decreased nucleation polarization (Fig. 2c) as well as improved adhesion ability (Fig. 2f) compared with the PCNF and Cu substrates.

To investigate the effect of Au@PCNF on the reversible Mg plating/stripping processes, we fabricated a 2032-type-coin cell by assembling each substrate, separator, and Mg metal in sequence. Voltage profiles for the cells with Cu, PCNF, and Au@PCNF are presented in Fig. 4a–c. During the repeated Mg plating/stripping process, rapid capacity decay was observed for the Cu substrate (Fig. 4a). This result occurred because the loss of deposited Mg metal was uncontrollable with the Mg easily electrically isolated; therefore, the dead Mg lump resulted in fast coulombic efficiency (CE) decay (72.2% at 30 cycles). Compared with the Cu substrate, the PCNF resulted in slightly improved CEs, and the hysteresis gap between the plating and stripping voltages was also reduced (Fig. 4b). The Au@PCNF delivered the reversible Mg plating/stripping behaviors with the highest CEs as well as the lowest voltage gaps (Fig. 4c). These results imply that the regulated Mg plating route and its uniform distribution enabled the reversible Mg plating/stripping cycles. The favorably guided Mg deposition was achieved using the magnesiophilic Au NPs, which prevented the massive agglomeration on the top surface as well as losses of Mg deposits, thereby enhancing the reversibility of the Mg plating/stripping behavior.

The CEs upon prolonged cycling are compared in Fig. 4d. Although the PCNF-based substrates initially exhibited relatively lower CEs than that of the Cu substrate, they increased to high values of ~95% after a few activation cycles. The Cu substrate showed a sharp decrease in the CE after 10 cycles and fluctuations in the CE from 30 cycles because of the dead Mg deposits and their irreversible behaviors. Although the CEs of PCNF started to decrease gradually after 7 cycles, the Au@PCNF exhibited more stable cycling performance, demonstrating the advantages of magnesiophilic Au NPs. Fig. 4e shows the cycle performances using the various substrates at a higher current density of 1 mA/cm² with a limited capacity at 1 mAh/cm². Although voltage hysteresis gaps for the Cu substrate and PCNF gradually increased with prolonged

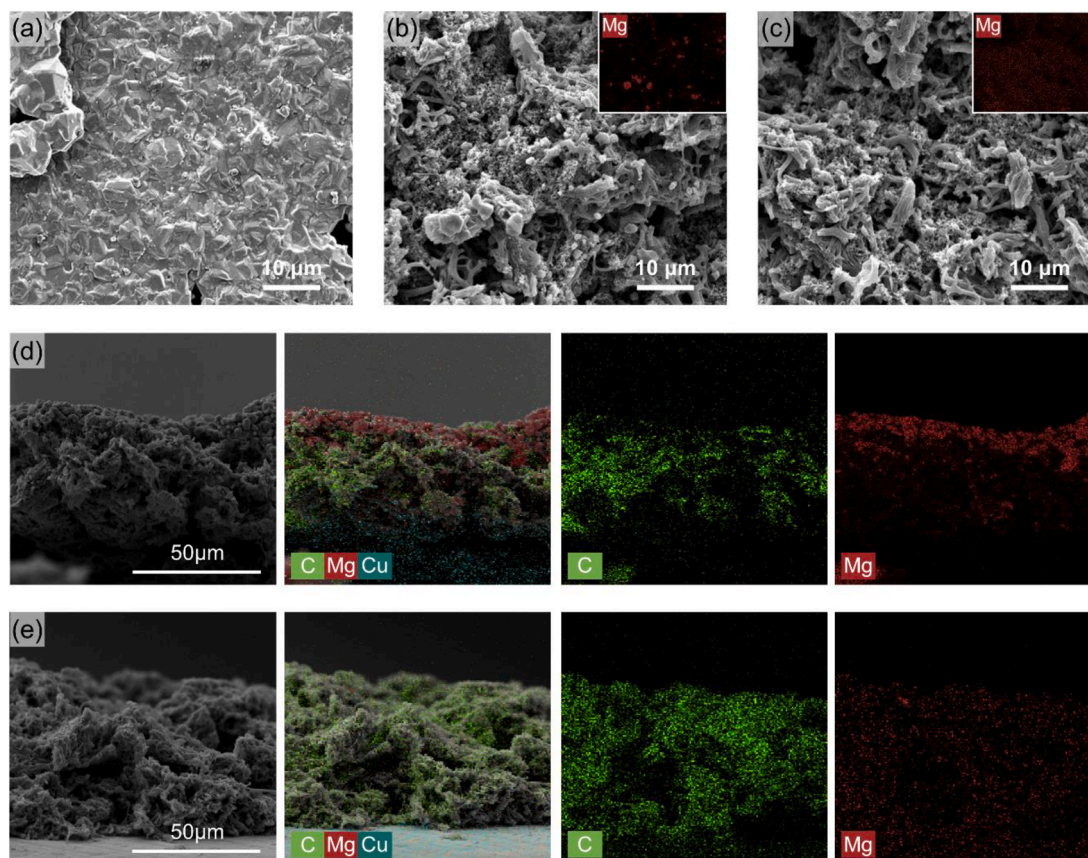


Fig. 3. SEM images after Mg deposition to 5 mAh/cm² at a current density of 0.2 mA/cm² on each substrate: (a) Cu, (b) PCNF, and (c) Au@PCNF. Cross-sectional SEM images and corresponding EDS mapping for (d) PCNF and (e) Au@PCNF substrates shown in (b–c).

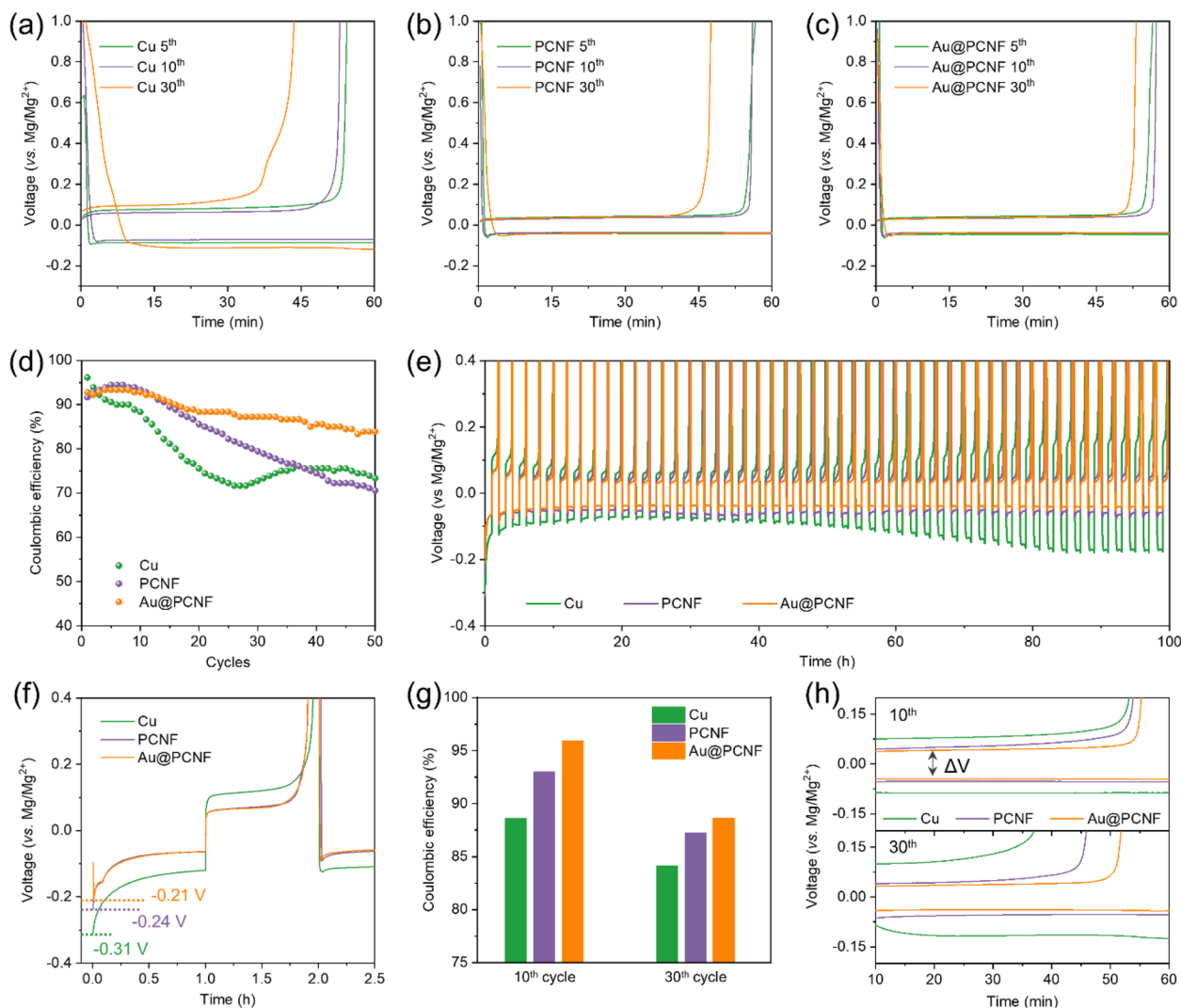


Fig. 4. Voltage profiles for Mg plating/stripping behaviors in half-cells using (a) Cu, (b) PCNF, and (c) Au@PCNF substrates at a current rate of 0.5 mA/cm^2 with a limited capacity of 0.5 mAh/cm^2 , and (d) CEs upon cycling. (e) Voltage–time curves for 50 cycles with a limited capacity of 1 mAh/cm^2 at a current rate of 1 mA/cm^2 and (f) expanded view of the voltage–time curves from 0 to 2.5 h. Corresponding (g) CEs at 10th and 30th cycles and (h) voltage hysteresis gaps.

cycling, Au@PCNF stably maintained its initial performance. The nucleation overpotentials for the initial plating correspond to -0.31 , -0.24 , and -0.21 V for the Cu substrate, PCNF, and Au@PCNF, respectively, as shown in Fig. 4f, and the trend (Cu > PCNF > Au@PCNF) matches well with the case operated at 0.2 mA/cm^2 (Fig. 2a–c). In other words, Au@PCNF presented the lowest nucleation overpotential for each cycle and exhibited the highest CE (Fig. 4g). Moreover, the voltage hysteresis gap (ΔV) of Mg deposition/stripping was reduced by using the PCNF-based substrates (Fig. 4h). The voltage hysteresis gap of the Cu substrate at 10 cycles was 0.167 V and was greatly increased to 0.232 V after 30 cycles. In contrast, the PCNF-based substrates exhibited much lower voltage hysteresis gaps (0.104 V for PCNF and 0.088 V for Au@PCNF) at the 10th cycle. For the Au@PCNF, the average voltage hysteresis gap after 30 cycles was only approximately 0.074 V , proving its reversible and efficient Mg-hosting ability. In addition, the capability of Au@PCNF as an anode was further investigated with a full cell test, and it showed a stable cyclability (Fig. S11). These results suggest that adopting a Mg anode host incorporating magnesiophilic seeds is an effective strategy for reversibly and efficiently accommodating Mg metal for advanced MMBs.

3. Conclusion

In this study, the unique structure of Au@PCNF, consisting of porous and hollow carbon nanofibers encapsulating Au NPs inside the core space, was designed to efficiently and reversibly accommodate Mg metal. The 3D PCNF-web body with hollow feature of Au@PCNF resulted in the facile transport of Mg ions together with greatly improved adhesion property of newly deposited Mg. We demonstrated that Au NPs showed high affinity toward Mg deposit, acting as magnesiophilic nucleation seeds, catalytically driving favorable and selective Mg deposition. As a result, even Mg deposition was successfully guided over the entire areas of Au@PCNF by preventing partial agglomerations and top-oriented plating; furthermore, the initial nucleation overpotential could be greatly reduced, resulting in long-term stable Mg plating/stripping performance. This approach is promising for the identification of a 3D structural host in combination with magnesiophilic nucleation seeds for developing efficient anode hosts for rechargeable MMBs.

4. Experimental section

4.1. Preparation

To synthesize the Au@PHCF, the core polymer solution was prepared by dissolving 30 wt% poly(styrene-co-acrylonitrile) (SAN, MW = 165000, Aldrich, USA) as a porogen and 0.15 wt% gold chloride (HAuCl₄, Aldrich, USA) in *N,N*-dimethylformamide (DMF, Aldrich, USA). The shell polymer solution was prepared by dissolving 9.2 wt% polyacrylonitrile (PAN, Aldrich, USA) and 2.3 wt% SAN in DMF. The core solution was connected to the inner channel of a dual nozzle (NNC-DN-1723, NanoNC, Korea), and the shell solution was connected to the outer channel. A voltage of 14 kV was applied, and the flow rates of the core and shell solution were 0.4 and 0.8 mL/h, respectively. The tip-to-drum collector distance was 20 cm. The collected as-electrospun fibers were carbonized to obtain Au@PCNF using a heat-treatment process under Ar atmosphere. To stabilize the PAN and melt the SAN polymer in the shell, the stabilization heat treatment was conducted at 280 °C for 1.5 h at a heating rate of 2 °C/min. The subsequent carbonization was then performed at 850 °C for 5 h at a ramping rate of 5 °C/min. The hollow PCNF was also prepared using the same procedure except with the addition of gold precursors.

The electrochemical cells for the Mg batteries were assembled in an Ar-filled glovebox (<1 ppm of O₂ and H₂O). A Mg-metal disk was scraped and polished on each side and assembled into a coin cell as rapidly as possible. All-phenyl complex (APC) electrolytes were prepared by mixing 133.3 mg of AlCl₃ and 1 mL of 2.0 M PhMgCl in tetrahydrofuran (THF) solution into 4 mL of THF solvent, which was pretreated with a molecular sieve (4 Å) overnight. To prepare the Au@PCNF substrate, a slurry of Au@PCNF, Super P carbon, and polyvinylidene fluoride in 1-methyl-2-pyrrolidinone in a weight ratio of 8:1:1 was used to coat the Cu foils. The coatings were dried overnight, and the foils were then placed in a vacuum oven at 80 °C. The substrates were punched into 12-mm disks to be assembled.

4.2. Characterization

The morphologies of the substrates were examined using SEM (Inspect F) and TEM (Titan TM 80–300). The Au-patterned Cu substrate was prepared by sputter deposition using a sputter coater (Hitachi, E-1045). The pore size distribution was determined by applying the Barrett–Joyner–Halenda (BJH) model using a porosity analyzer (Belsorp max, BEL). Nitrogen adsorption/desorption isotherms were obtained using a surface area analyzer (BELSORP-max, BEL, Japan). XRD with Cu K α radiation was used to analyze the crystal structure (D8 ADVANCE, Bruker). Thermogravimetric analysis was performed at a heating rate of 10 °C/min under air flow (SDT-Q600, TA Instruments). The electrochemical properties were measured using a potentiostat-galvanostat (WonAtech, WBCS 3000).

Declaration of Competing Interest

The authors declare that they have no known competing financial interests or personal relationships that could have appeared to influence the work reported in this paper.

Acknowledgments

This research was supported by the KIST Institutional Program (Project No. 2E30991) and a National Research Foundation of Korea (NRF) grant funded by the Korea government (MSIT) (No. 2021R1C1C1003628). B. G. Kim acknowledges support received from the Korea Electrotechnology Research Institute (KERI) Primary Research Program of MSIT/NST (21A01009).

Appendix A. Supplementary data

Supplementary data to this article can be found online at <https://doi.org/10.1016/j.cej.2021.133968>.

References

- [1] O. Schmidt, A. Hawkes, A. Gambhir, I. Staffell, The future cost of electrical energy storage based on experience rates, *Nat. Energy* 2 (2017) 1–8, <https://doi.org/10.1038/nenergy.2017.110>.
- [2] Y. Yang, E.G. Okonkwo, G. Huang, S. Xu, W. Sun, Y. He, On the sustainability of lithium ion battery industry—A review and perspective, *Energy Storage Mater.* 36 (2020) 186–212, <https://doi.org/10.1016/j.ensm.2020.12.019>.
- [3] Y. Cao, M. Li, J. Lu, J. Liu, K. Amine, Bridging the academic and industrial metrics for next-generation practical batteries, *Nat. Nanotechnol.* 14 (3) (2019) 200–207, <https://doi.org/10.1038/s41565-019-0371-8>.
- [4] J.W. Choi, D. Aurbach, Promise and reality of post-lithium-ion batteries with high energy densities, *Nat. Rev. Mater.* 1 (2016) 1–16, <https://doi.org/10.1038/natrevmats.2016.13>.
- [5] R. Schmuch, R. Wagner, G. Hörpel, T. Placke, M. Winter, Performance and cost of materials for lithium-based rechargeable automotive batteries, *Nat. Energy* 3 (4) (2018) 267–278, <https://doi.org/10.1038/s41560-018-0107-2>.
- [6] Y.-S. Hu, Batteries: getting solid, *Nat. Energy* 1 (2016) 1–2, <https://doi.org/10.1038/nenergy.2016.42>.
- [7] Y. Kato, S. Hori, T. Saito, K. Suzuki, M. Hirayama, A. Mitsui, M. Yonemura, H. Iba, R. Kanno, High-power all-solid-state batteries using sulfide superionic conductors, *Nat. Energy* 1 (2016) 1–7, <https://doi.org/10.1038/nenergy.2016.30>.
- [8] S. Randau, D.A. Weber, O. Kötz, R. Koerver, P. Braun, A. Weber, E. Ivers-Tiffée, T. Adermann, J. Kulisch, W.G. Zeier, F.H. Richter, J. Janek, Benchmarking the performance of all-solid-state lithium batteries, *Nat. Energy* 5 (3) (2020) 259–270, <https://doi.org/10.1038/s41560-020-0565-1>.
- [9] D. Aurbach, Z. Lu, A. Schechter, Y. Gofer, H. Gizbar, R. Turgeman, Y. Cohen, M. Moshkovich, E. Levi, Prototype systems for rechargeable magnesium batteries, *Nature* 407 (6805) (2000) 724–727, <https://doi.org/10.1038/35037553>.
- [10] P. Novák, R. Imhof, O. Haas, Magnesium insertion electrodes for rechargeable nonaqueous batteries—a competitive alternative to lithium? *Electrochim. Acta* 45 (1–2) (1999) 351–367, [https://doi.org/10.1016/S0013-4686\(99\)00216-9](https://doi.org/10.1016/S0013-4686(99)00216-9).
- [11] D.-T. Nguyen, R. Horia, A.Y.S. Eng, S.-W. Song, Z.W. Seh, Material design strategies to improve the performance of rechargeable magnesium-sulfur batteries, *Mater. Horiz.* 8 (3) (2021) 830–853, <https://doi.org/10.1039/D0MH01403F>.
- [12] J. Muldoon, C.B. Bucur, A.G. Oliver, T. Sugimoto, M. Matsui, H.S. Kim, G.D. Allred, J. Zajicek, Y. Kotani, Electrolyte roadblocks to a magnesium rechargeable battery, *Energy Environ. Sci.* 5 (2012) 5941–5950, <https://doi.org/10.1039/C2EE03029B>.
- [13] Y. Shao, T. Liu, G. Li, M. Gu, Z. Nie, M. Engelhard, J. Xiao, D. Lv, C. Wang, J.-G. Zhang, J. Liu, Coordination chemistry in magnesium battery electrolytes: how ligands affect their performance, *Sci. Rep.* 3 (1) (2013), <https://doi.org/10.1038/srep03130>.
- [14] Y.A. Wu, Z. Yin, M. Farmand, Y.-S. Yu, D.A. Shapiro, H.-G. Liao, W.-I. Liang, Y.-H. Chu, H. Zheng, In-situ multimodal imaging and spectroscopy of Mg electrodeposition at electrode-electrolyte interfaces, *Sci. Rep.* 7 (2017) 1–9, <https://doi.org/10.1038/srep42527>.
- [15] M. Jäckle, K. Helmbrecht, M. Smits, D. Stottmeister, A. Groß, Self-diffusion barriers: possible descriptors for dendrite growth in batteries? *Energy Environ. Sci.* 11 (12) (2018) 3400–3407, <https://doi.org/10.1039/C8EE01448E>.
- [16] M. Jäckle, A. Groß, Microscopic properties of lithium, sodium, and magnesium battery anode materials related to possible dendrite growth, *J. Chem. Phys.* 141 (17) (2014) 174710, <https://doi.org/10.1063/1.4901055>.
- [17] R. Attias, M. Salama, B. Hirsch, Y. Goffer, D. Aurbach, Anode-electrolyte interfaces in secondary magnesium batteries, *Joule* 3 (1) (2019) 27–52, <https://doi.org/10.1016/j.joule.2018.10.028>.
- [18] H. Shuai, J. Xu, K. Huang, Progress in retrospect of electrolytes for secondary magnesium batteries, *Coord. Chem. Rev.* 422 (2020) 213478, <https://doi.org/10.1016/j.ccr.2020.213478>.
- [19] M.M. Huie, D.C. Bock, E.S. Takeuchi, A.C. Marschilok, K.J. Takeuchi, Cathode materials for magnesium and magnesium-ion based batteries, *Coord. Chem. Rev.* 287 (2015) 15–27, <https://doi.org/10.1016/j.ccr.2014.11.005>.
- [20] R. Zhang, T.S. Arthur, C. Ling, F. Mizuno, Manganese dioxides as rechargeable magnesium battery cathode; synthetic approach to understand magnesiation process, *J. Power Sources* 282 (2015) 630–638, <https://doi.org/10.1016/j.jpowsour.2015.02.067>.
- [21] R. Zhang, C. Ling, Unveil the chemistry of olivine FePO₄ as magnesium battery cathode, *ACS Appl. Mater. Interfaces* 8 (28) (2016) 18018–18026, <https://doi.org/10.1021/acsami.6b03297>.
- [22] M.D. Regulacio, D.-T. Nguyen, R. Horia, Z.W. Seh, Designing Nanostructured Metal Chalcogenides as Cathode Materials for Rechargeable Magnesium Batteries, *Small* 17 (25) (2021) 2007683, <https://doi.org/10.1002/sml.v17.2510.1002/sml.202007683>.
- [23] R. Horia, D.-T. Nguyen, A.Y.S. Eng, Z.W. Seh, Using a Chloride-Free Magnesium Battery Electrolyte to Form a Robust Anode-Electrolyte Nanointerface, *Nano Lett.* 21 (19) (2021) 8220–8228, <https://doi.org/10.1021/acs.nanolett.1c02655>.
- [24] D.-T. Nguyen, A.Y.S. Eng, M.-F. Ng, V. Kumar, Z. Sofer, A.D. Handoko, G. S. Subramanian, Z.W. Seh, A High-Performance Magnesium Triflate-based

- Electrolyte for Rechargeable Magnesium Batteries, *Cell Rep. Phys. Sci.* 1 (12) (2020) 100265, <https://doi.org/10.1016/j.xcrp.2020.100265>.
- [25] R.E. Doe, R. Han, J. Hwang, A.J. Gmitter, I. Shterenberg, H.D. Yoo, N. Pour, D. Aurbach, Novel, electrolyte solutions comprising fully inorganic salts with high anodic stability for rechargeable magnesium batteries, *Chem. Commun.* 50 (2) (2014) 243–245, <https://doi.org/10.1039/C3CC47896C>.
- [26] T.D. Gregory, R.J. Hoffman, R.C. Winterton, Nonaqueous electrochemistry of magnesium: applications to energy storage, *J. Electrochem. Soc.* 137 (1990) 775.
- [27] M. Levi, E. Lancri, E. Levi, H. Gizbar, Y. Gofer, D. Aurbach, The effect of the anionic framework of Mo_6X_8 Chevrel Phase ($\text{X} = \text{S}, \text{Se}$) on the thermodynamics and the kinetics of the electrochemical insertion of Mg^{2+} ions, *Solid State Ion.* 176 (2005) 1695–1699, <https://doi.org/10.1016/j.ssi.2005.04.019>.
- [28] P. Saha, P.H. Jampani, M.K. Datta, D. Hong, B. Gattu, P. Patel, K.S. Kadakia, A. Manivannan, P.N. Kumta, A rapid solid-state synthesis of electrochemically active Chevrel phases (Mo_6T_8 ; $\text{T} = \text{S}, \text{Se}$) for rechargeable magnesium batteries, *Nano Res.* 10 (12) (2017) 4415–4435, <https://doi.org/10.1007/s12274-017-1695-z>.
- [29] P. Saha, P.H. Jampani, M.K. Datta, C.U. Okoli, A. Manivannan, P.N. Kumta, A convenient approach to Mo_6S_8 Chevrel phase cathode for rechargeable magnesium battery, *J. Electrochem. Soc.* 161 (4) (2014) A593–A598, <https://doi.org/10.1149/2.061404jes>.
- [30] M.S. Ding, T. Diemant, R.J. Behm, S. Passerini, G.A. Giffin, Dendrite growth in Mg metal cells containing $\text{Mg}(\text{TFSI})_2/\text{glyme}$ electrolytes, *J. Electrochem. Soc.* 165 (10) (2018) A1983–A1990, <https://doi.org/10.1149/2.1471809jes>.
- [31] H.-D. Lim, D.H. Kim, S. Park, M.E. Lee, H.-J. Jin, S. Yu, S.H. Oh, Y.S. Yun, Magnesiophilic Graphitic Carbon Nanosubstrate for Highly Efficient and Fast-Rechargeable Mg Metal Batteries, *ACS Appl. Mater. Interfaces* 11 (42) (2019) 38754–38761, <https://doi.org/10.1021/acsami.9b13447> [10.1021/acsami.9b13447](https://doi.org/10.1021/acsami.9b13447).s001.
- [32] K. Yan, Z. Lu, H.-W. Lee, F. Xiong, P.-C. Hsu, Y. Li, J. Zhao, S. Chu, Y. Cui, Selective deposition and stable encapsulation of lithium through heterogeneous seeded growth, *Nat. Energy* 1 (2016) 1–8, <https://doi.org/10.1038/nenergy.2016.10>.
- [33] V.S. Cvetković, N. Jovičević, J.S. Stevanović, M.G. Pavlović, N.M. Vukičević, Z. Stevanović, J.N. Jovičević, Magnesium–gold alloy formation by underpotential deposition of magnesium onto gold from nitrate melts, *Metals* 7 (2017) 95, <https://doi.org/10.3390/met7030095>.
- [34] Y. Takeda, T. Kuriwa, A. Kamegawa, M. Okada, Grain size refinements of Au-Mg alloy by hydrogen absorption/desorption treatments, *Mater. Trans.* 50 (3) (2009) 494–498, <https://doi.org/10.2320/matertrans.MBW200803>.
- [35] C. Yang, Y. Yao, S. He, H. Xie, E. Hitz, L. Hu, Ultrafine silver nanoparticles for seeded lithium deposition toward stable lithium metal anode, *Adv. Mater.* 29 (38) (2017) 1702714, <https://doi.org/10.1002/adma.201702714>.
- [36] C. Chen, J. Guan, N.W. Li, Y. Lu, D. Luan, C.H. Zhang, G. Cheng, L. Yu, X.W. Lou, Lotus-Root-Like Carbon Fibers Embedded with Ni-Co Nanoparticles for Dendrite-Free Lithium Metal Anodes, *Adv. Mater.* 33 (2021) 2100608, <https://doi.org/10.1002/202100608>.
- [37] Y. Fang, S.L. Zhang, Z.-P. Wu, D. Luan, X.W. Lou, A highly stable lithium metal anode enabled by Ag nanoparticle-embedded nitrogen-doped carbon macroporous fibers, *Sci. Adv.* 7 (2021) eabg3626, <https://doi.org/10.1126/sciadv.abg3626>.
- [38] Y. Fang, Y. Zeng, Q.i. Jin, X.F. Lu, D. Luan, X. Zhang, X.W. Lou, Nitrogen-Doped Amorphous Zn-Carbon Multichannel Fibers for Stable Lithium Metal Anodes, *Angew. Chem. Int. Ed.* 60 (15) (2021) 8515–8520, <https://doi.org/10.1002/anie.202100471>.
- [39] B.G. Kim, D.W. Kang, G. Park, S.H. Park, S.-M. Lee, J.W. Choi, Electrospun Li-confinable hollow carbon fibers for highly stable Li-metal batteries, *Chem. Eng. J.* 422 (2021) 130017, <https://doi.org/10.1016/j.cej.2021.130017>.